

Manufacturing complex Al₂O₃ ceramic structures using consumer-grade fused deposition modelling printers

N. A. Conzelmann^{1,2}, L. Gorjan², F. Sarraf³, L. D. Poulikakos², M. N. Partl², C. R. Müller¹, F. J. Clemens²

¹ ETH Zürich, Laboratory of Energy Science and Engineering, Department of Mechanical and Process Engineering, Institute of Energy Technology, Leonhardstrasse 21, 8092 Zürich, Switzerland

² Empa, Materials Science and Technology, Überlandstrasse 129, CH-8600 Dübendorf, Switzerland

Abstract

Purpose (limit 100 words)

The aim of this work was to fabricate complex ceramic tetrahedron structures, which are challenging to produce by more conventional methods such as injection molding. To achieve this aim, thermoplastic-ceramic composite filaments were developed and printed with unmodified, consumer-grade, fused deposition modelling (FDM) printers instead.

Design/methodology/approach

Al₂O₃ ceramic powder was mixed with ethylene vinyl acetate (EVA) polymer as a binder (50 vol.-%) to form a filament with a constant diameter of 1.75 mm. After the printing and thermal treatment stages, the shrinkage and mechanical properties of cuboid and tetrahedron structures were investigated.

Findings

The shrinkage of the parts was found to be anisotropic, depending on the orientation of the printing pattern, with an increase of 2.4% in the (vertical) printing direction compared to the (horizontal) printing layer direction. The alignment of the ceramic particle orientations introduced by FDM printing was identified as a potential cause of the anisotropy. This study further demonstrates that employing a powder bed during the thermal debinding process yields sintered structures that can withstand twice the compressive force.

Originality/value (limit 100 words)

Ceramic FDM had previously been used primarily for simple scaffold structures. In this study, the applicability of ceramic FDM was extended from simple scaffolds to more complex geometries such as hollow tetrahedra. The structures produced in this study contain dense parts printed from multiple contiguous layers, as compared to the open structures usually found in scaffolds. The mechanical properties of the complex ceramic parts made by employing this FDM technique were also subjected to investigation.

Keywords: Ceramic additive manufacturing; Ceramic 3D Printing; Complex Structures; Anisotropic shrinkage; Compressive Strength

1. Introduction

Fused deposition modelling (FDM) is a widely used, additive manufacturing technique for commercial as well as for consumer-grade applications, where it is colloquially known as 3D printing (Berman, 2012). Other labels for FDM can be found in the literature such as fused deposition of ceramics (FDC), extrusion freeform fabrication (EFF) and fused filament fabrication (FFF) (Grida and Evans, 2003; Rangarajan et al., 1997; Travitzky et al., 2014). The technique uses a thermoplastic feedstock which is extruded through a heated nozzle that follows a pre-programmed path. Complex geometries can be built by depositing multiple layers of material that overlay each other (Agarwala et al., 1996). After the extruded thermoplastic material leaves the nozzle, it fuses with the previously deposited material layer, before cooling and solidifying within seconds (Mohamed et al., 2015). This technique has been adapted for the production of ceramic parts by mixing the thermoplastic binder material with a ceramic powder (Danforth, 1995). Depending on the properties of the ceramic powder and the thermoplastic binder material, a powder content of 45 to 60 vol.-% is necessary in order for the printed parts to retain their shape during the subsequent debinding and sintering process (Clemens, 2009; Lewis, 1997).

While the FDM method for ceramics offers advantages with regard to the storability and flexibility of the filament, certain disadvantages have also been identified (Rangarajan et al., 1997). The difficulties in using FDM for ceramics arise from the necessity of removing the polymeric binder component from the printed part before sintering. Binder removal can lead to cracks and blisters in the final, sintered, ceramic parts, problems which are well known from other thermoplastic shaping processes for ceramics such as injection molding, thermoplastic extrusion and pressing (Bandyopadhyay and French, 1993; Enneti et al., 2012). Partial debinding with a solvent or super critical fluid can be used to avoid structural defects in the ceramic parts (Chartier et al., 1995). Alternatively, debinding in a powder bed can be used, where the capillary forces in action extract the liquid binder components and any decomposition products with a low viscosity from the part (Gorjan, 2012; Gorjan et al., 2015, 2017; Trunec and Cihlar, 2002), a process also referred to as wicking.

Previous work using the ceramic FDM technique was done by Bach et al. who printed piezoelectric scaffold structures from lead zirconate titanate and barium titanate (Bach et al., 2018). Further scaffold structures, some with functional materials, were manufactured by other researchers (Ho et al., 2002; Houmard et al., 2013; Jang et al., 2014). The effect of stearic acid on the stability of the 3D printed scaffold structures during thermal treatment was investigated by Gorjan et al. They used different grades of ethylene vinyl acetate (EVA), together with tricalcium phosphate (TCP) and stearic acid, in order to manufacture bio-ceramic scaffold structures (Gorjan et al., 2018). Another functional material was used by Rangarajan et al. who investigated the homogeneity of simple structures created by using the FDC method (Rangarajan et al., 1998). One of the observed results was anisotropic shrinkage, which occurred during the thermal treatment.

In this study we extend the applicability of ceramic FDM from simple scaffolds to more complex geometries such as hollow tetrahedra (see Figure 3A), which are difficult to produce by other methods such as injection molding. Such structures are interesting for use as granular packing material with a high, connected porosity, for example in catalytic applications like refractories, fixed bed reactors in the chemical industry, or porous asphalt (Nemec and Levec, 2005; Stempihar et al.,

2012). The structures manufactured in the course of this study contain dense parts printed from multiple contiguous layers, as compared to the open structures usually found in scaffolds. The industrial size of these applications demands keeping the processing stages as simple as possible. In the case of conventional polymer FDM it has already been previously shown that the printing direction can greatly influence the mechanical performance of the individual parts. For example, Ahn et al. found that specimens manufactured from ABS P400 polymer and compressed perpendicular to the printing layers had a 15% lower compressive strength when compared to specimens compressed parallel to the printing layers (Ahn et al., 2002). However, to the best of our knowledge, no investigation of the possible anisotropic mechanical properties of ceramic parts made by employing the FDM technique has been done up to date. In this work we study the anisotropic properties of ceramic FDM structures with complex geometries. The shrinkage of structures during thermal treatment is investigated in respect of the printing direction and their mechanical properties are investigated by means of compression tests.

2. Methods

An outline illustrating the development steps and investigations performed during this study is shown in Figure 1. The feedstock composition was developed and evaluated with regard to its suitability for FDM. Cuboid samples were simultaneously manufactured using the FDM technique in order to perform a preliminary investigation of the influence of printing parameters such as the amount of infill on the properties of the samples during thermal treatment as well as the compression strength. The experience gained from these preliminary investigations was finally employed to manufacture complex tetrahedron structures, which were subsequently evaluated in respect of their performance during thermal treatment and mechanical testing.

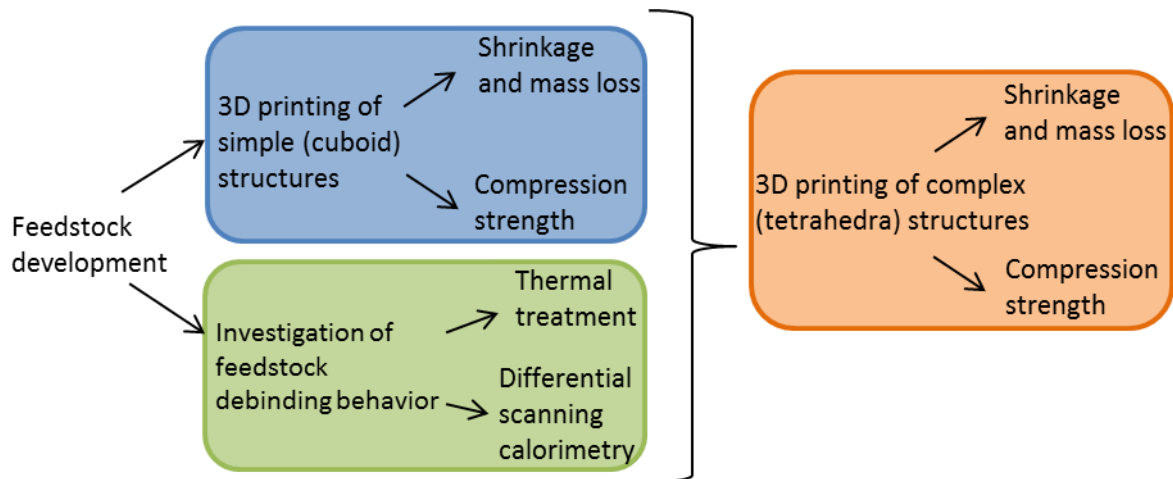


Figure 1: Schematic depicting the development steps and investigations performed during this study

The feedstock was developed on the basis of the experience obtained in previous studies (Gorjan et al., 2018). An alumina powder loading of 50 vol.-% was chosen. A filament with a low powder content has a lower viscosity, which can cause buckling at the printing head during 3D printing. A high powder content increases the viscosity of the feedstock, thus increasing the risk of clogging the 3D printer nozzle. The alumina powder used was Al_2O_3 (CT 3000 LS SG, Almatix GmbH) with a mass median diameter (D50) of 0.5 μm . CT 3000 LS SG is an oxide material widely used in ceramic research (Beresnev et al., 2014; Chovanec et al., 2012; Károly et al., 2014; Lauria et al., 2016; Melcher et al., 2011; Polsakiewicz and Kollenberg, 2011; Río et al., 2017; Zorzi et al., 2002). The binder consisted of

ethylene-vinyl acetate co-polymer (EVA) (Elvax 420™, DuPont International SARL) with a melting point of 73 °C and a melt flow rate of 150 g/10 min. In addition, stearic acid (Sigma Aldrich) was added as a surfactant. The exact formulation of the feedstock is shown in Table 1.

Table 1: Feedstock formulation used in this study.

Component	Volume [%]	Density [g/cm³]	Mass [%]
EVA	40.9	0.93	15.6
Stearic acid	9.1	0.85	3.2
Alumina	50.0	3.97	81.3

The thermoplastic EVA-Al₂O₃ compound was mixed in a two-step procedure, using a high shear mixer (Rheomix 600, HAAKE PolyLab OS, Thermo Electron Corporation Inc.) with roller rotors. In the first step, pre-mixing was performed at a temperature of 80 °C and a speed of 10 rpm for 20 minutes. After pre-mixing, the high shear mixer was emptied and cleaned to eliminate any unmixed zones from the chamber. In the second step, the material was mixed at 80 °C and a speed of 10 rpm for 20 minutes and then the speed was increased to 40 rpm for another 20 minutes. The feedstock was extruded with a piston extruder (RH7 Flowmaster, Malvern Instruments Ltd) using a circular die (diameter 1.75 mm) and at a temperature of 70 °C to create a filament for 3D printing with a consumer-grade FDM printer (K8200 3D printer, Velleman NV). The printing process was performed using a brass nozzle with a diameter of 0.6 mm and at a constant temperature of 170 °C. The extrusion multiplier, which defines the volumetric fraction of the feedstock being fed into the nozzle and extruded, was set to 0.9. This value is <1 since the feedstock slightly expands after leaving the nozzle. The layer height, i.e. the distance from the nozzle to the previously deposited layer of material, was set to 0.5 mm. The printing speed, which defines the maximal velocity with which the nozzle traverses horizontally while material is being extruded, was set to 800 mm/min.

The geometric information was imported as stereolithography (.stl) files into the Simplify3D software, which is used to slice the geometry into layers and determine the tooling path for each layer. A visualization of the tooling path for the square cuboid samples can be found in Figure 2A and Figure 2B. Figure 2 further shows two different cuboid orientations (upright Figure 2C and recumbent Figure 2D) used during printing. The printing direction (PD) denotes the direction in which the layers are stacked whereas the layer direction (LD) denotes the horizontal plane in which the printing tool moves during the creation of an individual layer. The printed cuboids have a length (*l*) of 15 mm and a width (*w*) of 3.54 mm independent of the printing orientation. Regardless of the geometry, the tool path first follows the contour of the object to be printed in order to create the surface. When a hollow sample is printed, the print head moves upwards and prints the next layer, which is in turn generated from the contour of the geometry (Figure 2A). When printing a sample with infill, the contour is printed first, as with the hollow sample. Before the next layer is deposited on top, the inside of the layer is filled with a predefined structure. This structure, for example a rectilinear grid of variable density, can be defined by the operator (Figure 2B).

After printing, the cuboid samples in this study were thermally treated according to the program shown in Figure 4, without the use of a powder bed, in order to keep the thermal treatment as simple as possible.

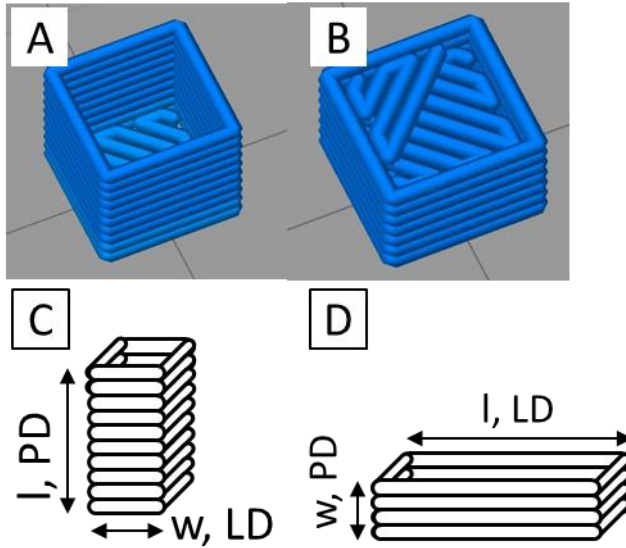


Figure 2: A/B) Visualization of tooling paths for the 3D printing of the cuboids, created using Simplify3D software. A) Hollow cuboid printed upright. B) Completely filled (100% infill) cuboid printed upright. C) Sketch of a cuboid sample printed in upright position. D) Sketch of a cuboid printed in recumbent position. PD denotes the vertical printing direction in which the layers are stacked, whereas LD denotes the horizontal layer direction in which individual layers are created. The length and width of the cuboid are denoted by l and w , respectively.

Using the knowledge gained in making these cuboids, the fabrication of more complex shapes, in this case tetrahedra, was undertaken next. The tetrahedron shape consisted of six connected cylinders with a diameter of 3 mm and a length (c) of 20 mm with rounded ends, which were oriented along the edges of the tetrahedron, resulting in a height (h) of 16.33 mm. An image of this shape can be seen in Figure 3A. Due to the symmetry of a tetrahedron we can observe four different heights with equal length on a printed tetrahedron. One of these heights corresponds to the PD while the other three correspond to the other directions (OD). The tetrahedra were manufactured with three horizontal cylinders positioned flat on the printing platform while the remaining three cylinders were built upright on top of the lower three. After investigation of the printed cuboid structures, an infill comprised of a rectilinear grid with a porosity of 50% was selected for the manufacture of the tetrahedron. The tooling path for the three horizontal cylinders which form the base of the tetrahedron is shown in Figure 3B. The tooling path for the three upright cylinders is shown in Figure 3C (the blue hollow cylinders). Each of the tetrahedron's cylinders has a diameter of 3 mm, but the nozzle for printing the samples has a diameter of 0.6 mm. This leads to a thickness of contour of the shape of at least 0.6 mm. A single pass of the nozzle through the interior would already fill the remaining space by more than 50% (see Figure 3C). Therefore, the interior remains empty and the vertical cylinders of the tetrahedron remain hollow. This design problem does not occur in the horizontal cylinders forming the lower triangle of the tetrahedron shape. These layers have a shape resembling two concentric triangles, which leaves enough room to print a rectilinear grid with a 50% infill (Figure 3B). For debinding and sintering, the tetrahedra were placed in two different orientations: upright, which is the printing orientation (Figure 3D), and upended so that the PD was at an angle of 19.47° to the horizontal plane (Figure 3E). This was done to investigate shrinkage independently of any deformation due to the tetrahedron's own weight.

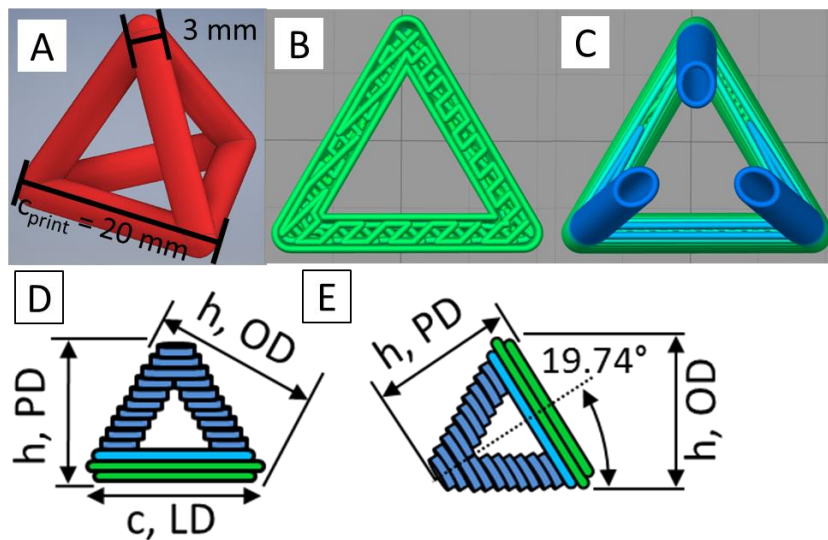


Figure 3: A) Image of the tetrahedron geometry to be printed. B) Horizontally printed cylinder parts of the tetrahedron, printed with a 50% infill of rectilinear grid structure. C) Vertically printed cylinder parts of the tetrahedron, printed without infill. The color indicates the printing speed (green is faster than blue). For debinding and sintering, the tetrahedra were placed in different positions in a furnace. D) Sketch of the layer orientation of a printed tetrahedron sample (the printing direction (PD) is vertical, this orientation is "upright" throughout the manuscript). The direction of the individual layers is denoted LD. E) Sketch of a tetrahedron sample upended so that the PD is at an angle of 19.47° to the horizontal plane. The height of a tetrahedron which does not correspond to the PD is labelled "other direction" (OD).

Thermal treatment of the printed samples was done in three stages. The first two stages, partial debinding and pre-sintering, were done in a PC12 furnace (Pyrotek GmbH) with a TC 405/30 controller (bentrup Industriesteuerungen). The third thermal treatment stage (sintering) was performed at 1600 °C in an air atmosphere for one hour using an LT 40/12 furnace (Nabertherm GmbH). After each stage, the samples were cooled down to room temperature by shutting off the oven in order to permit further analysis. Partial debinding was done at 230 °C for 8 hours unless otherwise stated, whilst full debinding and pre-sintering was done at 1000 °C for two hours. The pre-sintered samples were sufficiently robust to allow transfer to the high temperature oven for sintering. The complete temperature profile for all stages of the thermal treatment is shown in Figure 4. The cuboid samples were thermally treated in a recumbent position and placed on a solid surface. Upright printed cuboid samples were brought into a recumbent position for their thermal treatment. Overall, six different tetrahedra were investigated: three were thermally treated without a powder bed and three were partially debound and pre-sintered in a powder bed, thus facilitating the extraction of the binder using capillary forces (Kim et al., 1999). Two of the tetrahedra were thermally treated in an upended position so that the printing direction was at a 19.47° angle to the horizontal plane (Figure 3E); one with and one without a powder bed. The powder bed consisted of Al_2O_3 (Nabalox NO 201, Nabaltec, Germany) with a mass median diameter (D50) of 80 μm .

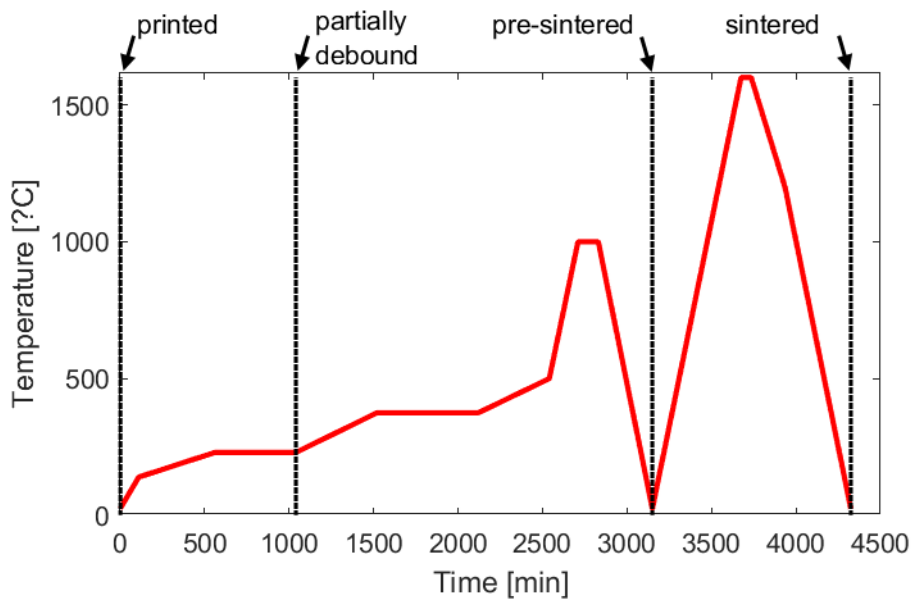


Figure 4: Temperature profile of the full thermal treatment for each of the 3D printed parts. The dotted vertical lines indicate the stages at which samples were inspected for further analysis.

For the thermogravimetric analysis (TGA) of the decomposition of the EVA binder in air, a STA 449 F3 Jupiter (Netzsch GmbH) thermal analyzer was used, together with pieces of the 1.75 mm thick filament. Thermo-mechanical analysis (TMA) of the cuboid samples was performed by using a TMA 402 F3 Hyperian (Netzsch GmbH) and heating them to 1550 °C in air. During the TMA measurements the samples were in an upright position and a static force of 0.1 N was applied in the vertical direction. Mechanical testing of the sintered parts was done using a universal testing machine (UPM 1478, ZwickRoell GmbH & Co. KG). The force was applied uniaxially in the vertical direction by means of placing rigid, flat plates placed on both sides. The surface of the sintered samples manufactured using FDM is uneven. Therefore, the steel plates on both ends were padded with cardboard and rubber to ensure that the applied force was distributed evenly. During the experiments the samples were compressed uniaxially at a constant speed of 4 mm/min until the failure of a sample which led to a sudden drop in the compressive force. At that point compression was stopped. The tetrahedron samples were mechanically tested in the same position as that in which they had been thermally treated (upright or upended). Scanning electron microscope (SEM) images were acquired with a VEGA3 (Tescan a.s.).

3. Results and Discussion

3.1 Development of printable filaments and thermal treatment

Once the samples are 3D printed, the thermoplastic binder must be removed (debinding stage). Figure 5 shows the TGA-DSC analysis of the filament samples. For the analysis, 2 mm-long pieces of the extruded filament with a diameter of 1.75 mm were used. Then two different heating programs were implemented, one with and one without the optimized debinding process stage. Figure 5A shows the heat treatment at a constant heating rate of 5 °C/min up to 600 °C. In Figure 5B the debinding program has been optimized for this study. The optimized program was used for all samples throughout this study. The binder starts to decompose at temperatures above 170 °C, as indicated by the mass loss seen in the TGA analysis of both samples. For the sample shown in Figure 5A, a sudden decrease of mass can be observed at a temperature of 322 °C and again at 433 °C. This sudden decrease of mass coincides with a strong exothermic peak in the DSC graph. The sudden loss

of mass also leads to the formation of defects in the ceramic part (Hrdina et al., 1998). When the optimized debinding program is used, the exothermic peak can be reduced significantly and a more continuous loss of mass can be observed during the debinding stage, as shown in Figure 5B. The optimized debinding program is characterized by slower heating rates and additional dwell times for a gentler binder removal which mitigates the aforementioned formation of defects (Gorjan, 2012). The final mass loss of the samples was 19.0% (Figure 5A) and 18.8% (Figure 5b). These values are close to the total content of the organic binder, (18.8%) based on the feedstock composition used (see Table 1).

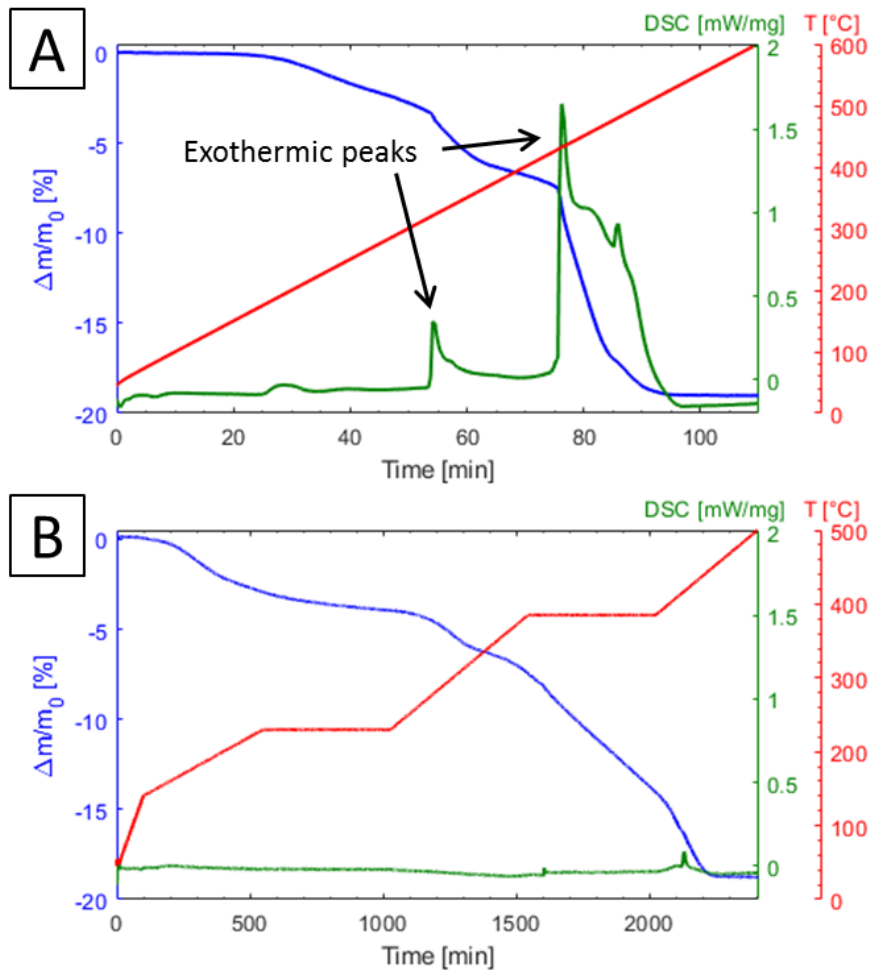


Figure 5: Results of the thermogravimetric analysis of the debinding process stage used to remove thermoplastic binder and organic surfactant from a filament sample. The temperature profile is shown in red while the change in mass is shown in blue. The differential scanning calorimetry (DSC) is shown in green. A) Sample heated at a constant heating rate of 5 °C/min. B) Sample heated with an optimized debinding program.

3.2 3D printed cuboid structures: thermal treatment and mechanical properties

Figure 6 shows images of the 3D printed and sintered cuboids for each of the four configurations (recumbent 100% infill, recumbent 0% infill, upright 100% infill and upright 0% infill). Four samples were used to investigate shrinkage and mass loss after the different thermal treatment stages (Figure 4). After sintering, the cuboids with 100% infill exhibited slightly convex surfaces. This can be attributed to gas transport from the center to the surface of the sample during the decomposition of the thermoplastic binder. If this gas transport is limited, pressure inside the sample will result in the expansion of the sample (Hrdina et al., 1998). Such an expansion is shown in Figure 6A and Figure 6C, where the swelling is indicated with black arrows.

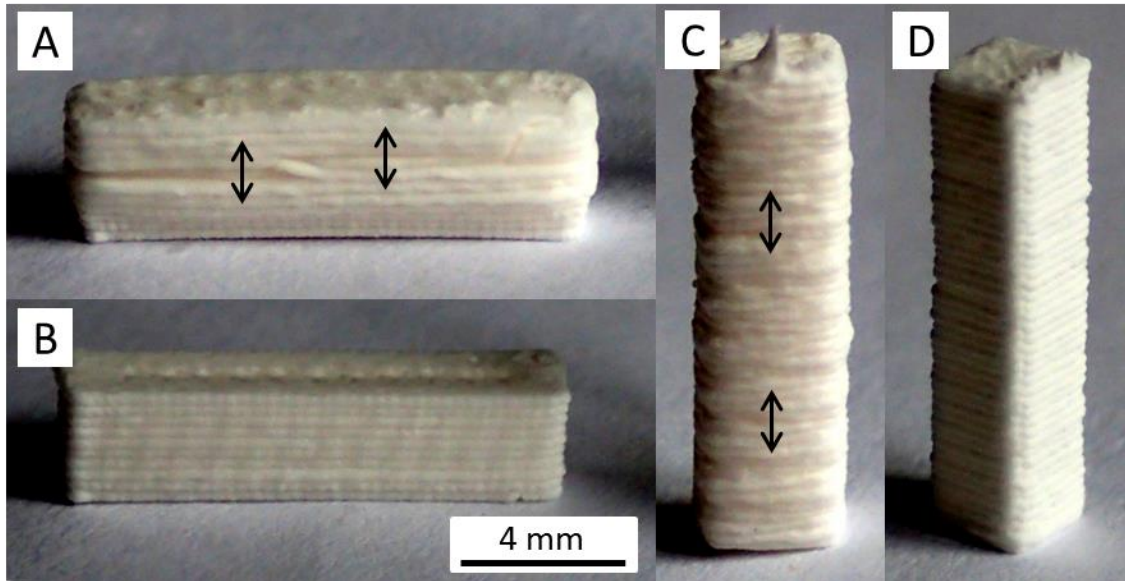


Figure 6: Images of 3D printed cuboids after sintering. A) Printed with 100% infill in recumbent position. The direction of expansion (swelling) observable in samples with 100% infill is denoted by black arrows. B) Printed hollow (0% infill) and in recumbent position. C) Printed upright with 100% infill. D) Printed with 0% infill in upright position. The scale bar is valid for all subfigures.

Figure 7A shows a cracked sample printed with 100% infill after sintering. The sample has irregular, internal void structures, which are a result of the decomposition of the thermoplastic binder. This observation corroborates the assumption that the decomposition of the binder leads to an increase in gas pressure, which forms bubbles inside the samples. Hrdina et al. proposed that the decomposition of EVA leads to the formation of acetic acid, which bloats the specimen (Hrdina et al., 1999) This bloating in turn explains the swelling of the samples printed with 100% infill, as shown in Figure 6A and Figure 6C. Such an expansion could be avoided in samples with a 0% infill print parameter (Figure 7B).

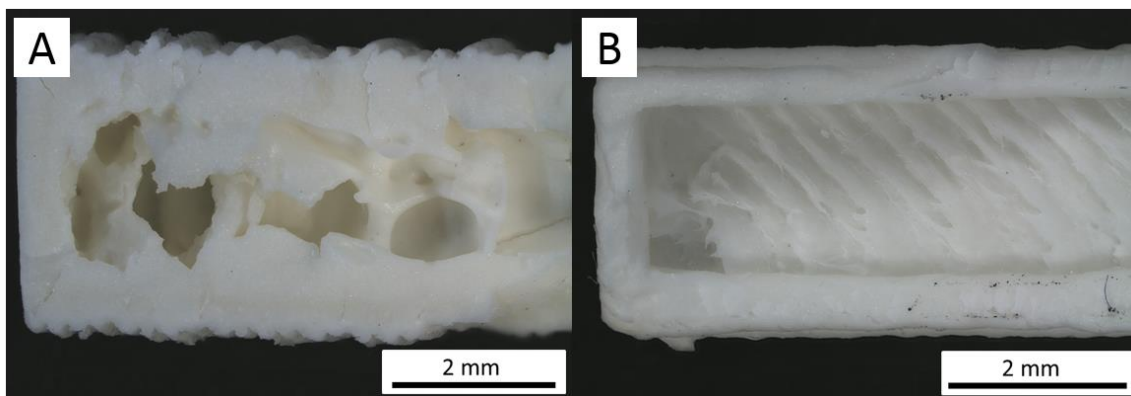


Figure 7: Microscopy images showing the inside of fragments of cuboid samples which cracked along their length. A) Sample printed with 100% infill. B) Sample printed with 0% infill.

Thermal mechanical analysis was used to investigate the shrinkage of the cuboids during the sintering process. Due to the softening of the polymeric binder (EVA and stearic acid), the shrinkage up to and including the pre-sintering stage cannot be analyzed using a dilatometer or TMA. Typically, a small load is applied between the sample and the TMA probe to ensure continuous contact. Therefore, deformation would occur due to the softening of the thermoplastic EVA binder during

TMA while debinding. It should be noted that the temperature range of the TMA used is limited to a maximum of 1550 °C and therefore full densification is not to be expected. The results of the TMA are shown in Figure 8. From this data (up to 1000° C) the coefficient of thermal expansion (CTE) for Al_2O_3 can be determined as being $8.7 \cdot 10^{-6} \text{ 1/K}$. The sintering of the CT3000 started at a temperature of 1086 °C and a heating rate of 3 °C/min. Vogt et al. performed dilatometry measurements using a heating rate of 5 °C/min and observed that the sintering of CT 3000 started at 981 °C (Vogt et al., 2010). The temperature at which the sintering process started shifted in the present study in comparison to the findings of Vogt et al. because a pre-sintering stage was employed. During sintering the sample measured in the LD direction has a slightly lower shrinkage value in comparison to the sample in the PD direction. This indicates that the printing direction has a significant effect on the total shrinkage of the sample and anisotropic shrinkage can be expected in structures printed by FDM. During the cooling process both samples shrank by an additional 1.34%, which corresponds to a CTE of $8.7 \cdot 10^{-6} \text{ 1/K}$. Munro previously reported a similar CTE of $8.1 \cdot 10^{-6} \text{ 1/K}$ for polycrystalline Al_2O_3 at 1000 °C (Munro, 1997).

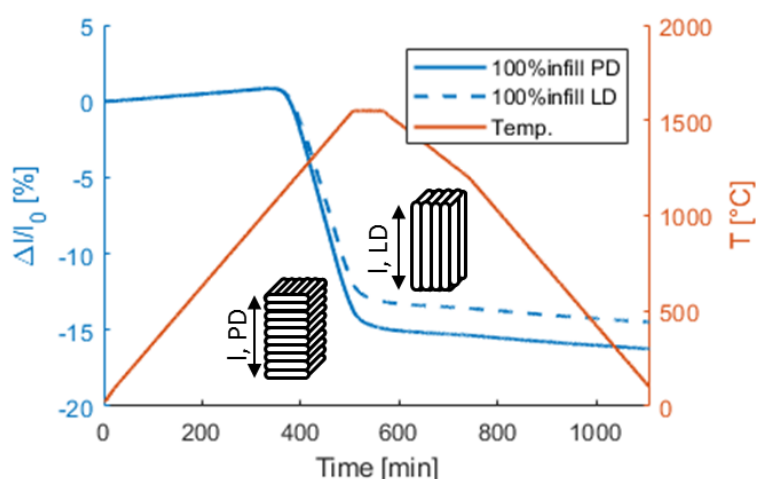


Figure 8: Thermomechanical analysis showing the shrinkage of cuboid samples printed with 100% infill in recumbent (measured along the LD) and upright position (measured in the PD).

In addition to the TGA and TMA analysis, mass loss and shrinkage of the cuboids were analyzed using an analytical scale and calipers after each thermal treatment stage. Figure 9A shows the shrinkage and the results of the mass loss analysis for the four configurations of cuboids (upright, measured in the PD, with 0% infill, recumbent, measured in the LD, with 0% infill, upright (PD) 100% infill and recumbent (LD) 100% infill). The data was averaged over all four samples of a respective configuration. In order to analyze the shrinkage, the length (l) of each cuboid was measured, which can correspond to either the PD or the LD, depending on whether the sample was printed upright or recumbent. The labels on the graphs indicate whether the PD or the LD was measured.

During the partial debinding stage, the samples with a 100% infill lost $3.4 \pm 0.2\%$ (\pm one standard deviation) of their total mass (LD and PD) while the samples with 0% infill lost $4.5 \pm 0.2\%$ and $4.9 \pm 0.3\%$ of their total mass for the LD and PD orientation respectively. The reason for the higher mass loss of samples with 0% infill compared to samples with 100% infill is that the samples are less massive. In hollow samples the distance which the evaporating polymer needs to diffuse before escaping is shorter (Trunec and Cihlar, 2002). Furthermore, in the case of debinding in air, reactions with oxygen occur and the binder is transformed into a hard brown resin on the surface (Gorjan et al., 2012). This leads to the formation of a dense skin on the surface, which hinders the transport of gaseous species and consequently leads to a pressure build-up which can cause cracking and bloating (Gorjan et al.,

2018; Zorzi et al., 2002). The formation of such a dense skin depends on the diffusion of oxygen into the samples.

In the TGA analysis (Figure 5B) a loss of 4.0% of the total mass has been observed after partial debinding (at the end of the 8h dwell time at 230 °C). Since the length and diameter of the TGA samples are smaller than the dimensions of the cuboid samples, the diffusion processes of the decomposition products have less significance and therefore a higher mass loss is to be expected. The influence of the diffusion process on the mass loss during partial debinding can be confirmed by cuboid samples with 0% and 100% infill. The mass loss of the TGA sample of 4.0% during partial debinding is closer to the mass loss of the cuboid samples with 0% infill ($4.5 \pm 0.2\%$ LD and $4.9 \pm 0.3\%$ PD) than to that of the samples with 100% infill ($3.4 \pm 0.2\%$). Similar results have been reported by Trunec et al. who reported that the binder mass loss at 230 °C increases with increasing surface to volume ratio (Trunec and Cihlar, 2002).

After the pre-sintering stage at 1000 °C, all organics had decomposed, resulting in an overall mass loss of $19.0 \pm 0.9\%$ averaged over all four sample configurations. This value corresponds to the average overall mass loss of the two TGA samples (19.0% and 18.8%) and the theoretical content of the organic material in the feedstock at 18.8% (see Table 1 and Figure 5). No further mass loss should occur during the sintering stage, which is confirmed by the constant average mass of the samples between the pre-sintering and sintering stage shown in Figure 9A.

The shrinkage data of the samples (Figure 9) shows that the most significant changes occur during sintering. During partial debinding and pre-sintering the samples shrank between $1.2 \pm 0.6\%$ (0% infill PD) and $1.6 \pm 0.5\%$ (100% infill LD). The shrinkages reported here are generally higher than the net shrinkage of 0.5% observed by Hrdina et al (Hrdina and Halloran, 1998) during binder removal. In their study, an EVA based binder blended with 51vol.-% of ceramic powder was used and shrinkage was studied at 500 °C. Due to the fragility of the samples, the cuboids had to be heat-treated at 1000 °C, which resulted in higher shrinkage values compared to Hrdina et al. due to the effects of pre-sintering.

One exception is the 100% infill PD sample which was printed in an upright position, where an increase in length by $0.1 \pm 0.6\%$ and $1.0 \pm 1.1\%$ could be observed after the partial debinding and pre-sintering processes respectively. A possible explanation for this expansion in the PD is that the gas arising from the decomposing binder pushes the elongated ceramic particles apart while escaping the sample. Such particles can be seen in Figure 10A. This SEM image shows that the CT 3000 LS SG powder used in this study contains a mixture of submicron particles and 2 µm large platelet particles. During extrusion in the 3D printer, these elongated platelet particles become aligned due to shear in the nozzle (Börzsönyi et al., 2012; Nagy et al., 2017; Patterson et al., 2017). Consequently, the elongated particles are aligned in LD, which is also illustrated in Figure 10B. Figure 10B further shows a gap d between the particles, which is filled with binder. When evaporating binder escapes the sample, these gaps expand. Assuming the gaps expand by equal amounts, one can envision from Figure 10B that the relative expansion in the LD is larger than in the PD. After binder decomposition the particles become locked into their positions. This prevents a full reversal of the expansion. The measured expansions are in well in line with the observed expansion of 100% infill samples after sintering (Figure 6A/C). Interestingly, such an expansion could not be observed for the 100% infill samples in the LD. This corroborates the theory proposed in Figure 10B.

The shrinkage of the cuboids during sintering was normalized by the length after the pre-sintering stage and is shown separately in Figure 9B. Samples with 100% infill printed in a recumbent position (measured in the LD) shrank by $14.6 \pm 0.2\%$ and the samples printed upright (measured in the PD) shrank by $14.7 \pm 0.8\%$. At $16.1 \pm 0.6\%$ for the samples measured in the LD and at $18.5 \pm 0.8\%$ for those in

the PD, the normalized shrinkage of the hollow samples is considerably higher. From this observation it can be deduced that the normalized shrinkage is generally higher for samples with 0% infill as compared to 100% infill samples. As already discussed for the TMA analysis (Figure 8), the shrinkage is anisotropic. For the 0% infill cases studied, the PD direction shrinks by an additional 2.4% compared to the LD direction. This cannot be observed in the 100% infill samples since these samples are affected by the internal voids formed during the binder decomposition.

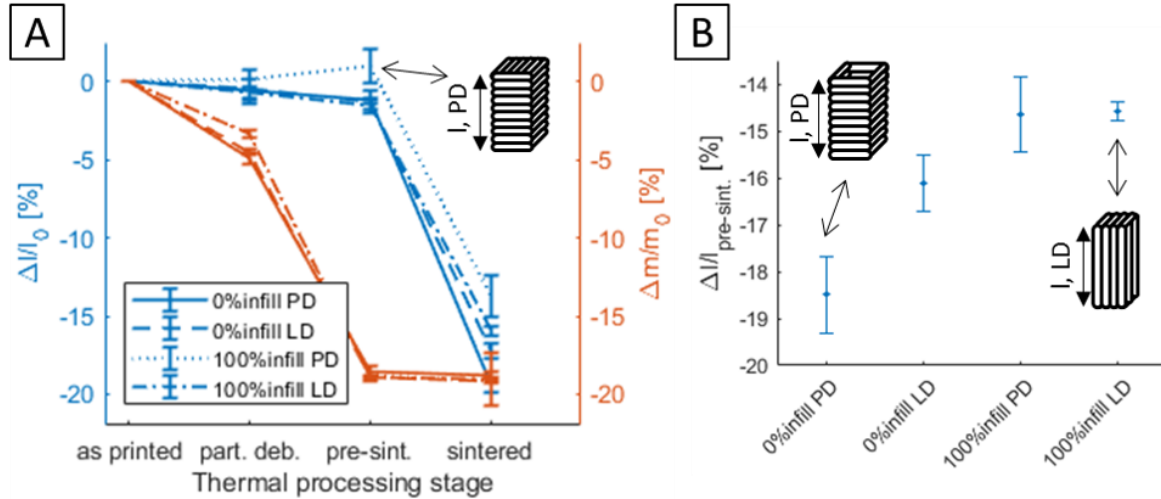


Figure 9: A) In blue: Average shrinkage of the cuboid samples during the different thermal treatment stages for the four different printing configurations (upright 0% infill (PD), recumbent 0% infill (LD), upright 100% infill (PD) and recumbent 100% infill (LD)) measured along the length of the samples. In orange: The average change of the samples during the different thermal treatment stages. B) The amount of shrinkage occurring during the final sintering stage relative to the pre-sintering length.

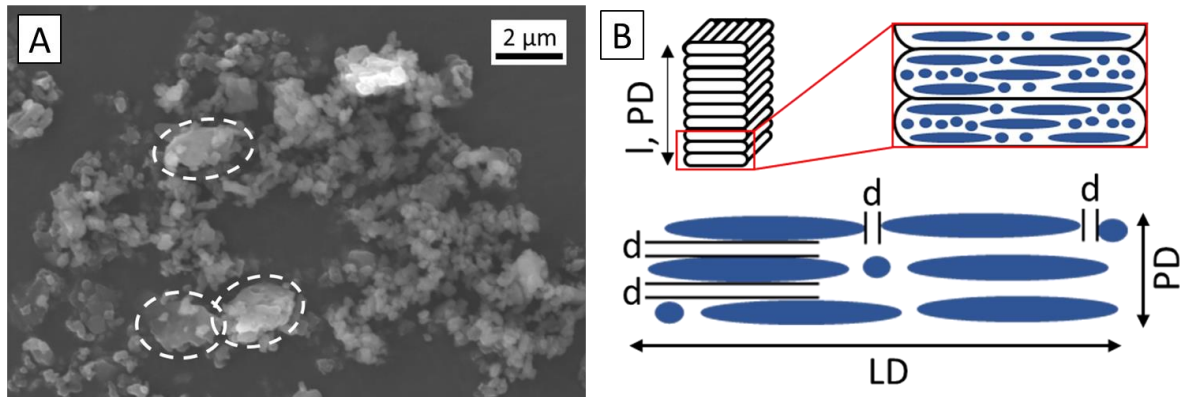


Figure 10: A) SEM image of CT 3000 LS SG powder used in this study showing some large platelet particles (dashed white circles). B) Schematic explaining how the platelet particles contribute to the anisotropic expansion of samples during debinding.

As mentioned above, anisotropic expansion during debinding as well as anisotropic shrinkage during sintering was observed. According to the morphology of the CT 3000 LS SG alumina, which consist of slightly elongated submicron and platelet-like micro particles, the ceramic particles become aligned during the extrusion of the filament and the 3D printing. The orientation of the particles causes the expansion and shrinkage to be anisotropic.

The maximal compressive load of the different cuboid structures was evaluated by compression tests. The results of the three samples tested for each configuration are shown in Figure 11: Compression force for the four different configurations of cuboid structures. The black bars depict the

average value of the three samples analyzed. Figure 11, together with the averages. One can see that the samples compressed along the LD show slightly higher values when compared with samples with the same infill percentage tested in the PD. A similar observation was made by Ahn et al. for 3D printed acrylonitrile butadiene styrene (ABS) polymer samples (Ahn et al., 2002). Figure 7 shows that, due to the formation of voids from the decomposing binder, the load-bearing cross-section is not considerably higher for the sample printed with 100% infill after sintering. Therefore, the average load at failure is only slightly lower for samples with 0% infill compared to samples with 100% infill with the same configuration.

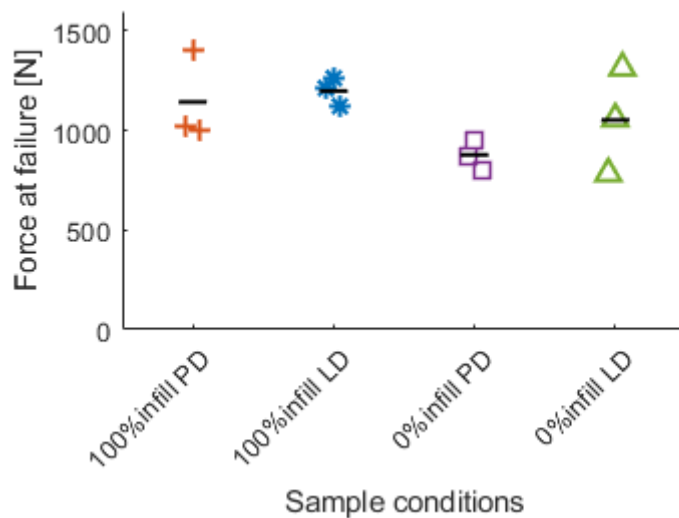


Figure 11: Compression force for the four different configurations of cuboid structures. The black bars depict the average value of the three samples analyzed.

3.3 3D printed tetrahedron structures: thermal treatment and mechanical properties

The knowledge gained from manufacturing the simple geometry of the cuboid samples was used directly in the production of the tetrahedron structures created using the FDM/FFF 3D printing method. Figure 12 shows tetrahedron structures and their transformation during the fabrication process after printing (Figure 12A), partial debinding (Figure 12B), pre-sintering (Figure 12C) and finally after sintering (Figure 12D). It was observed that the shape and surface quality do not change significantly until the pre-sintered stage (Figure 12C). The sintered samples decrease in size and the surface is considerably smoother, with less roughness (Figure 12D). The brown discoloration during the partial debinding stage (Figure 12B) is due to the oxidation and decomposition of the thermoplastic binder (Gorjan et al., 2012; Trunec and Cihlar, 2002; Zorzi et al., 2002). This discoloration is related to the previously mentioned hard skin. It is suggested in the literature that this brown skin consists of products arising from the oxidation and thermal decomposition of the organic binder.

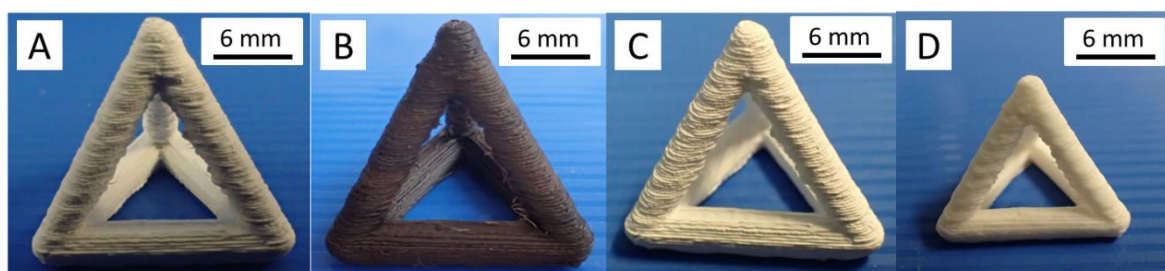


Figure 12: Tetrahedron-shaped part at different stages of the thermal treatment. A) As printed, B) after partial debinding, C) pre-sintered and D) fully sintered.

In order to assure shape stability, an infill of 50% had to be used in the printing of the tetrahedron samples. Some samples were placed in a powder bed to avoid expansion of the 50% infill parts in the tetrahedron due to gas pressure during the partial debinding stage. With the aid of capillary forces, the decomposed binder could be actively removed from the sample surface. Gorjan et al. have shown that, due to capillary forces, parts of a thermoplastic binder can be efficiently removed by use of a wicking process at 230 °C (Gorjan et al., 2017). Figure 13 shows the shrinkage data (blue graph) of all horizontally oriented cylinders after the individual thermal treatment stages. During partial debinding some samples were treated with and some without a powder bed. In addition, upended samples (see Figure 3C) were partially debound under both conditions. Furthermore, the mass loss for all experiments is shown in by the orange graph in Figure 13.

In addition, Figure 13 shows that samples treated in a powder bed initially lost a larger fraction of their total mass during the partial debinding stage compared to the samples treated without a powder bed ($5.3 \pm 0.1\%$ versus $4.0 \pm 0.02\%$). These values show that capillary forces indeed enhanced binder removal. The total mass loss of $4.0 \pm 0.02\%$ in tetrahedra debound without a powder bed lies between the mass loss of cuboid structures with 100% infill ($3.4 \pm 0.2\%$) and cuboid structures with 0% infill ($4.5 \pm 0.2\%$ LD and $4.9 \pm 0.3\%$ PD). This result is consistent with tetrahedra having an infill percentage of 50% in the horizontal cylinders and 0% in the vertical cylinders. At the fully sintered stage, the samples treated in a powder bed and the samples treated without a powder bed had a total mass loss of $18.8 \pm 0.02\%$ and $19.2 \pm 0.1\%$ respectively, which is in the range of values obtained for cuboids and the theoretical mass loss of the feedstock composition.

The shrinkage of tetrahedra during debinding with and without a powder bed was investigated by measuring the length of each of the horizontal cylinders (corresponding to the LD) in the four samples with a caliper. The data shown as the blue line in Figure 13 suggests a slightly increased shrinkage for samples debound in a powder bed compared to samples debound without a powder bed. During debinding without a powder bed, the cylinders of the tetrahedra shrank by $1.8 \pm 0.7\%$. This value is comparable to the shrinkage of the cuboid structures in the LD (0% infill $1.2 \pm 0.6\%$; 100% infill $1.6 \pm 0.5\%$) which were likewise debound without a powder bed. The cylinders of tetrahedra debound in a powder bed shrank by $2.2 \pm 0.6\%$. After sintering, the final shrinkage in samples debound in a powder bed was $17.8 \pm 1.6\%$ as opposed to $18.3 \pm 2.0\%$ in samples debound without a powder bed. These results are well in line with the shrinkage of cuboids with 0% infill when measured in the LD direction ($17.2 \pm 0.5\%$).

Figure 14 compares the heights of the different tetrahedron configurations during the thermal treatment stages. In accordance with Figure 3, the heights of the tetrahedra were analyzed in the printing direction (PD) and in other directions (OD). Samples were partially debound with and without a powder bed. As already mentioned, the total shrinkage of tetrahedra partially debound in an upright position is not affected by the use of a powder bed. During partial debinding, upright and

upended samples shrank by $2.5 \pm 1.3\%$ and $2.4 \pm 0.3\%$ respectively in the PD. For the OD, shrinkage of $1.6 \pm 0.5\%$ (upright) and $1.8 \pm 0.5\%$ (upended) was analyzed. The total shrinkage of the PD in upright and upended orientation is $20.9 \pm 0.4\%$ and $17.2 \pm 0.4\%$, respectively. Since the PD and OD shrinkage values are equal regardless of the orientation of the tetrahedra during thermal treatment, deformation of the tetrahedra due to their own weight can be disregarded. Furthermore, the total shrinkage in the OD is in good agreement with the total shrinkage of the cuboids with 0% infill measured in LD ($17.2 \pm 0.5\%$). As expected of the cuboids with 0% filling (total shrinkage of $19.5 \pm 0.5\%$), a larger shrinkage is to be observed in the PD. The anisotropy shown in these results can be explained with the non-random orientation of ceramic particles.

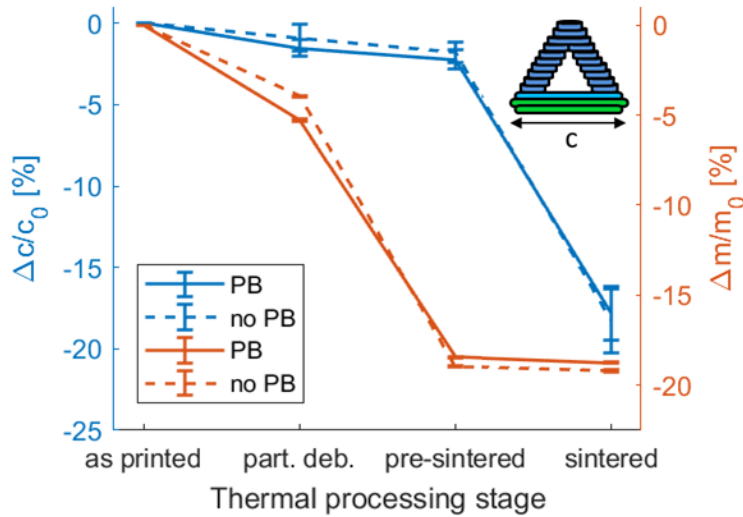


Figure 13: Shrinkage and mass loss of tetrahedra after different thermal treatment stages. Blue graph: Length c of the printed tetrahedra samples during thermal treatment with powder bed (PB) and without powder bed (no PB). The powder bed was employed only during partial debinding and pre-sintering. Orange graph: mass loss of the tetrahedra during thermal treatment stages.

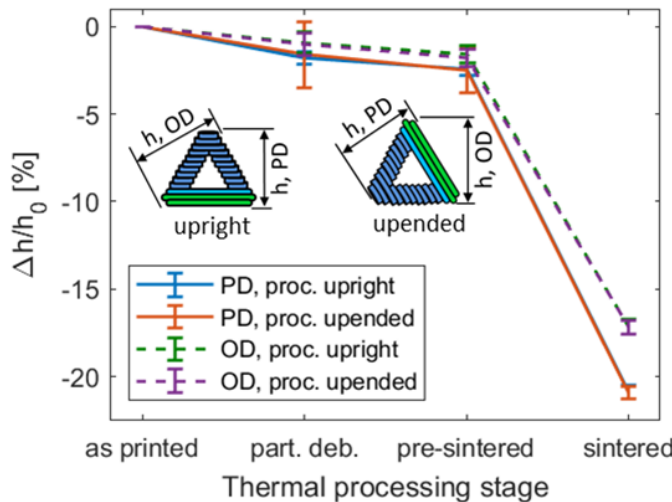


Figure 14: Shrinkage of tetrahedra that have been thermal treated in different positions. Heights (h) of tetrahedra, which correspond either to the print direction (PD) or the other directions (OD). The tetrahedra were either thermally treated in the upright direction in which they were printed (see Figure 3D) or upended so the PD was no longer vertical (see Figure 3E).

Figure 15 shows the force-displacement curves of the compression tests for the tetrahedra in different configurations and with different treatments. The samples were compressed from the top in the same orientation (upright/upended) that was used during the thermal treatment of each sample (see Figure 3C/D). The tetrahedra which were partially debound in a powder bed had a force at failure that was two times higher in comparison to those partially debound without a powder bed. This suggests that debinding without a powder bed introduced defects that negatively affected the mechanical strength of the structures. Additional investigations on filament samples which were debound using the same thermal treatment as with the tetrahedra confirmed this. Several major as well as minor cracks could be observed inside filament samples debound without a powder bed. In filament samples debound with the use of a powder bed we observed that the magnitude and number of such cracks was greatly reduced. Images of the cross-sections of such filament samples can be found in the supplementary information (Figure S2 and Figure S3). Unexpectedly, the orientation of the samples (e.g. upright or upended) did not affect the force at failure.

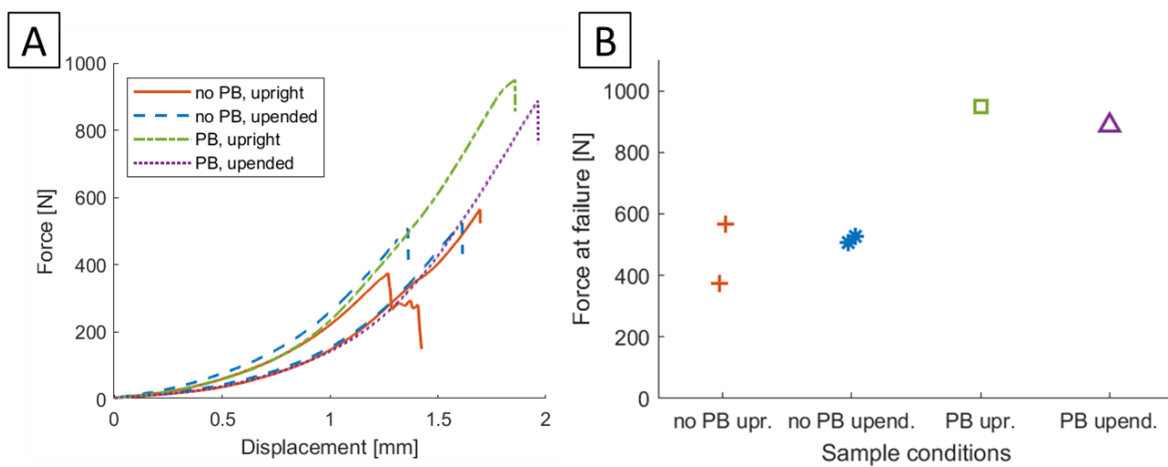


Figure 15: A) Force-displacement curve of tetrahedra during uniaxial compression tests. The samples were compressed vertically in the same orientation with regard to the layer structure as previously employed (see Figure 3D/E and Figure 14). B) The maximal force at failure of the tetrahedra samples.

4. Conclusions

The thermoplastic alumina feedstock prepared as part of this study was successfully used to produce tetrahedron structures by means of a consumer grade FDM printer. This extends the applicability of ceramic FDM from simple scaffold structures to complex structures with multiple contiguous layers. An optimized thermal debinding program for an EVA-based binder system was developed. Slower heating rates and dwell times were introduced to the debinding program to reduce exothermic events which could lead to defects in the parts. It was found that the shrinkage of parts during thermal treatment is anisotropic. Cuboids with 0% infill show increased shrinkage of 2.4% in the (vertical) printing direction compared to the (horizontal) layer direction. This result could be confirmed by analyzing the shrinkage of tetrahedra, where the printing direction shrank 3.7% more in comparison to the layer direction. From these results, we can deduce that ceramic structures manufactured using an FDM method show anisotropic shrinkage, which needs to be taken into account during the design of such structures. According to the morphology of the CT 3000 LS SG ceramic powder, the ceramic particles can be expected to obtain a preferential alignment during extrusion. Such an alignment of particles during the manufacturing of ceramic structures will result in anisotropic shrinkage. Further investigations with other ceramic powders will have to be done to confirm the relevance of process-related anisotropic shrinkage for other ceramic materials.

Compression tests show that cuboid samples with 100% infill fail at roughly the same force as cuboids with 0% infill. This can be attributed to a reduction of the load-bearing cross-section of structures with 100% infill due to the formation of internal voids during debinding. The influence of the printing orientation on the mechanical properties was found to be minor. However, tetrahedra partially debound in a powder bed could withstand twice the compressive force compared to tetrahedra which were partially debound without a powder bed.

Acknowledgments

The authors would like to thank the Swiss National Science Foundation (SNF) for the financial support with the project number SNF 200021_157122/11 and funding for the analytic instrument SNF 206021_64024. The authors would also like to thank Tobias Rantze for his continuing support with the 3D printer and fruitful discussions and Roland Bächtold for his help with the setup for the compression tests. The support of Markus Zwick who provided the SEM image of the CT 3000 LS SG powder is greatly appreciated.

References

- Agarwala, M.K., Jamalabad, V.R., Langrana, N.A., Safari, A., Whalen, P.J. and Danforth, S.C. (1996), "Structural quality of parts processed by fused deposition", *Rapid Prototyping Journal*, MCB UP Ltd, Vol. 2 No. 4, pp. 4–19.
- Ahn, S.H., Montero, M., Odell, D., Roundy, S. and Wright, P.K. (2002), "Anisotropic material properties of fused deposition modeling ABS", *Rapid Prototyping Journal*, MCB UP Ltd, Vol. 8 No. 4, pp. 248–257.
- Bach, M., Sebastian, T., Melnykowycz, M., Lusiola, T., Scharf, D. and Clemens, F. (2018), "Additive Manufacturing of Piezoelectric 3-3 Composite Structures", *Industrializing Additive Manufacturing - Proceedings of Additive Manufacturing in Products and Applications - AMPA2017*, Springer International Publishing, Cham, pp. 93–103.
- Bandyopadhyay, G. and French, K.W. (1993), "Injection-molded ceramics: Critical aspects of the binder removal process and component fabrication", *Journal of the European Ceramic Society*, Elsevier, Vol. 11 No. 1, pp. 23–34.
- Beresnev, V.M., Smolyakova, M.Y., Pogrebnyak, A.D., Kaverina, A.S., Drobyshevskaya, A.A., Svetlichnyy, E.A. and Kolesnikov, D.A. (2014), "Studying tribological characteristics of alumina- and zirconia-based ceramics", *Journal of Friction and Wear*, Allerton Press, Vol. 35 No. 2, pp. 137–140.
- Berman, B. (2012), "3-D printing: The new industrial revolution", *Business Horizons*, Elsevier, Vol. 55 No. 2, pp. 155–162.
- Börzsönyi, T., Szabó, B., Törös, G., Wegner, S., Török, J., Somfai, E., Bien, T., et al. (2012), "Orientational Order and Alignment of Elongated Particles Induced by Shear", *Physical Review Letters*, American Physical Society, Vol. 108 No. 22, p. 228302.
- Chartier, T., Ferrato, M. and Baumard, J.F. (1995), "Supercritical Debinding of Injection Molded Ceramics", *Journal of the American Ceramic Society*, Wiley/Blackwell (10.1111), Vol. 78 No. 7, pp. 1787–1792.
- Chovanec, J., Galusek, D., Ráheľ, J. and Šajgalík, P. (2012), "Low loss alumina dielectrics by aqueous tape casting: The influence of composition on the loss tangent", *Ceramics International*,

Elsevier, Vol. 38 No. 5, pp. 3747–3755.

- Clemens, F. (2009), "Thermoplastic Extrusion for Ceramic Bodies", *Extrusion in Ceramics*, Springer, Berlin, Heidelberg, pp. 295–311.
- Danforth, S. (1995), "Fused Deposition of Ceramics: A New Technique for the Rapid Fabrication of Ceramic Components", *Materials Technology*, Taylor & Francis, Vol. 10 No. 7–8, pp. 144–146.
- Enneti, R.K., Park, S.J., German, R.M. and Atre, S. V. (2012), "Review: Thermal Debinding Process in Particulate Materials Processing", *Materials and Manufacturing Processes*, Taylor & Francis Group, Vol. 27 No. 2, pp. 103–118.
- Gorjan, L. (2012), "Wick Debinding - An Effective Way of Solving Problems in the Debinding Process of Powder Injection Molding", *Some Critical Issues for Injection Molding*, InTech, available at: <https://doi.org/10.5772/34969>.
- Gorjan, L., Blugan, G., Graule, T. and Kuebler, J. (2015), "Effectiveness of wick-debinding inside powder bed for ceramic laminates made by tape casting", *Powder Technology*, Elsevier, Vol. 273, pp. 197–202.
- Gorjan, L., Dakskobler, A. and Kosmač, T. (2012), "Strength Evolution of Injection-Molded Ceramic Parts During Wick-Debinding", edited by Menon, M. *Journal of the American Ceramic Society*, Wiley/Blackwell (10.1111), Vol. 95 No. 1, pp. 188–193.
- Gorjan, L., Lusiola, T., Scharf, D. and Clemens, F. (2017), "Kinetics and equilibrium of Eco-debinding of PZT ceramics shaped by thermoplastic extrusion", *Journal of the European Ceramic Society*, Elsevier, Vol. 37 No. 16, pp. 5273–5280.
- Gorjan, L., Reiff, L., Liersch, A. and Clemens, F. (2018), "Ethylene vinyl acetate as a binder for additive manufacturing of tricalcium phosphate bio-ceramics", *Ceramics International*, Elsevier, Vol. 44 No. 13, pp. 15817–15823.
- Grida, I. and Evans, J.R.G. (2003), "Extrusion freeforming of ceramics through fine nozzles", *Journal of the European Ceramic Society*, Elsevier, Vol. 23 No. 5, pp. 629–635.
- Ho, S.L., Yang, S.F., Chua, C.K., Leong, K.F., Cheah, C.M., Too, M.H. and Du, Z.H. (2002), "Investigation of 3D Non-Random Porous Structures by Fused Deposition Modelling", *The International Journal of Advanced Manufacturing Technology*, Vol. 19 No. 3, pp. 217–223.
- Houmard, M., Fu, Q., Genet, M., Saiz, E. and Tomsia, A.P. (2013), "On the structural, mechanical, and biodegradation properties of HA/ β -TCP robocast scaffolds", *Journal of Biomedical Materials Research Part B: Applied Biomaterials*, Wiley-Blackwell, Vol. 101 No. 7, pp. 1233–1242.
- Hrdina, K.E. and Halloran, J.W. (1998), "Dimensional changes during binder removal in a mouldable ceramic system", *Journal of Materials Science*, Kluwer Academic Publishers, Vol. 33 No. 11, pp. 2805–2815.
- Hrdina, K.E., Halloran, J.W., Kaviany, M. and Oliveira, A. (1999), "Defect formation during binder removal in ethylene vinyl acetate filled system", *Journal of Materials Science*, Kluwer Academic Publishers, Vol. 34 No. 13, pp. 3281–3290.
- Hrdina, K.E., Halloran, J.W., Oliveira, A. and Kaviany, M. (1998), "Chemistry of removal of ethylene vinyl acetate binders", *Journal of Materials Science*, Kluwer Academic Publishers, Vol. 33 No. 11, pp. 2795–2803.
- Jang, D.-W., Franco, R.A., Sarkar, S.K. and Lee, B.-T. (2014), "Fabrication of porous hydroxyapatite scaffolds as artificial bone preform and its biocompatibility evaluation.", *ASAIO Journal (American Society for Artificial Internal Organs : 1992)*, Wolters Kluwer Health, Vol. 60 No. 2, pp. 216–23.

- Károly, Z., Balázs, C., Balázs, K., Petrik, A., Lábár, J. and Dhar, A. (2014), "Hybride aluminum matrix composites prepared by spark plasma sintering (SPS)", *European Chemical Bulletin*, Vol. 3 No. 3, pp. 247–250.
- Kim, S.W., Lee, H.-W. and Song, H. (1999), "Effect of minor binder on capillary structure evolution during wicking", *Ceramics International*, Elsevier, Vol. 25 No. 7, pp. 671–676.
- Lauria, I., Kramer, M., Schröder, T., Kant, S., Hausmann, A., Böke, F., Leube, R., et al. (2016), "Inkjet printed periodical micropatterns made of inert alumina ceramics induce contact guidance and stimulate osteogenic differentiation of mesenchymal stromal cells", *Acta Biomaterialia*, Elsevier, Vol. 44, pp. 85–96.
- Lewis, J.A. (1997), "Binder Removal from Ceramics", *Annual Review of Materials Science*, Annual Reviews, Vol. 27 No. 1, pp. 147–173.
- Melcher, R., Travitzky, N., Zollfrank, C. and Greil, P. (2011), "3D printing of Al₂O₃/Cu–O interpenetrating phase composite", *Journal of Materials Science*, Springer US, Vol. 46 No. 5, pp. 1203–1210.
- Mohamed, O.A., Masood, S.H. and Bhowmik, J.L. (2015), "Optimization of fused deposition modeling process parameters: a review of current research and future prospects", *Advances in Manufacturing*, Springer, Vol. 3 No. 1, pp. 42–53.
- Munro, R.G. (1997), "Evaluated Material Properties for a Sintered alpha-Alumina", *Journal of the American Ceramic Society*, John Wiley & Sons, Ltd (10.1111), Vol. 80 No. 8, pp. 1919–1928.
- Nagy, D.B., Claudin, P., Börzsönyi, T. and Somfai, E. (2017), "Rheology of dense granular flows for elongated particles", *Physical Review E*, American Physical Society, Vol. 96 No. 6, p. 062903.
- Nemec, D. and Levec, J. (2005), "Flow through packed bed reactors: 1. Single-phase flow", *Chemical Engineering Science*, Pergamon, Vol. 60 No. 24, pp. 6947–6957.
- Patterson, G.A., Fierens, P.I., Sangiuliano Jimka, F., König, P.G., Garcimartín, A., Zuriguel, I., Pugnali, L.A., et al. (2017), "Clogging Transition of Vibration-Driven Vehicles Passing through Constrictions", *Physical Review Letters*, American Physical Society, Vol. 119 No. 24, p. 248301.
- Polsakiewicz, D.A. and Kollenberg, W. (2011), "Highly loaded alumina inks for use in a piezoelectric print head", *Materialwissenschaft Und Werkstofftechnik*, John Wiley & Sons, Ltd, Vol. 42 No. 9, pp. 812–819.
- Rangarajan, S., Pozsgai, I., McIntosh, J., McCuiston, R., Harper, B.L., Langrana, N., Safari, A., et al. (1998), "Homogeneity, Anisotropy, and Texture In Si₃N₄ Ceramics made by Fused Deposition", *MRS Proceedings*, Cambridge University Press, Vol. 542, p. 97.
- Rangarajan, S., Qi, G., Bandyopadhyay, A., Dai, C., Han, J.W., Bharagava, P., Wu, S., et al. (1997), "The role of materials processing variables in FDC process", *Proceedings Of the Solid Freeform Fabrication Symposium*, Vol. 4 No. 4, pp. 431–440.
- Río, F. del, Boado, M.G., Rama, A. and Guitián, F. (2017), "A comparative study on different aqueous-phase graphite exfoliation methods for few-layer graphene production and its application in alumina matrix composites", *Journal of the European Ceramic Society*, Elsevier, Vol. 37 No. 12, pp. 3681–3693.
- Stempihar, J.J., Pourshams-Manzouri, T., Kaloush, K.E. and Rodezno, M.C. (2012), "Porous Asphalt Pavement Temperature Effects for Urban Heat Island Analysis", *Transportation Research Record: Journal of the Transportation Research Board*, SAGE PublicationsSage CA: Los Angeles, CA, Vol. 2293 No. 1, pp. 123–130.
- Travitzky, N., Bonet, A., Dermeik, B., Fey, T., Filbert-Demut, I., Schlier, L., Schlördt, T., et al. (2014),

“Additive Manufacturing of Ceramic-Based Materials”, *Advanced Engineering Materials*, Vol. 16 No. 6, pp. 729–754.

Trunec, M. and Cihlar, J. (2002), “Thermal removal of multicomponent binder from ceramic injection mouldings”, *Journal of the European Ceramic Society*, Elsevier, Vol. 22 No. 13, pp. 2231–2241.

Vogt, U.F., Gorbar, M., Dimopoulos-Eggenschwiler, P., Broenstrup, A., Wagner, G. and Colombo, P. (2010), “Improving the properties of ceramic foams by a vacuum infiltration process”, *Journal of the European Ceramic Society*, Elsevier, Vol. 30 No. 15, pp. 3005–3011.

Zorzi, J.E., Perottoni, C.A. and Da Jornada, J.A.H. (2002), “Hard-skin development during binder removal from Al₂O₃-based green ceramic bodies”, *Journal of Materials Science*, Vol. 37 No. 9, pp. 1801–1807.

Supplementary information

Figure S1 shows a cross-section of the green filament which was used in the 3D printing. The filament is generally homogeneous. The rough surface on the top right and along the edge of the filament stems from the breaking of the filament. Cutting the filament leads to an even rougher surface than cracking however.

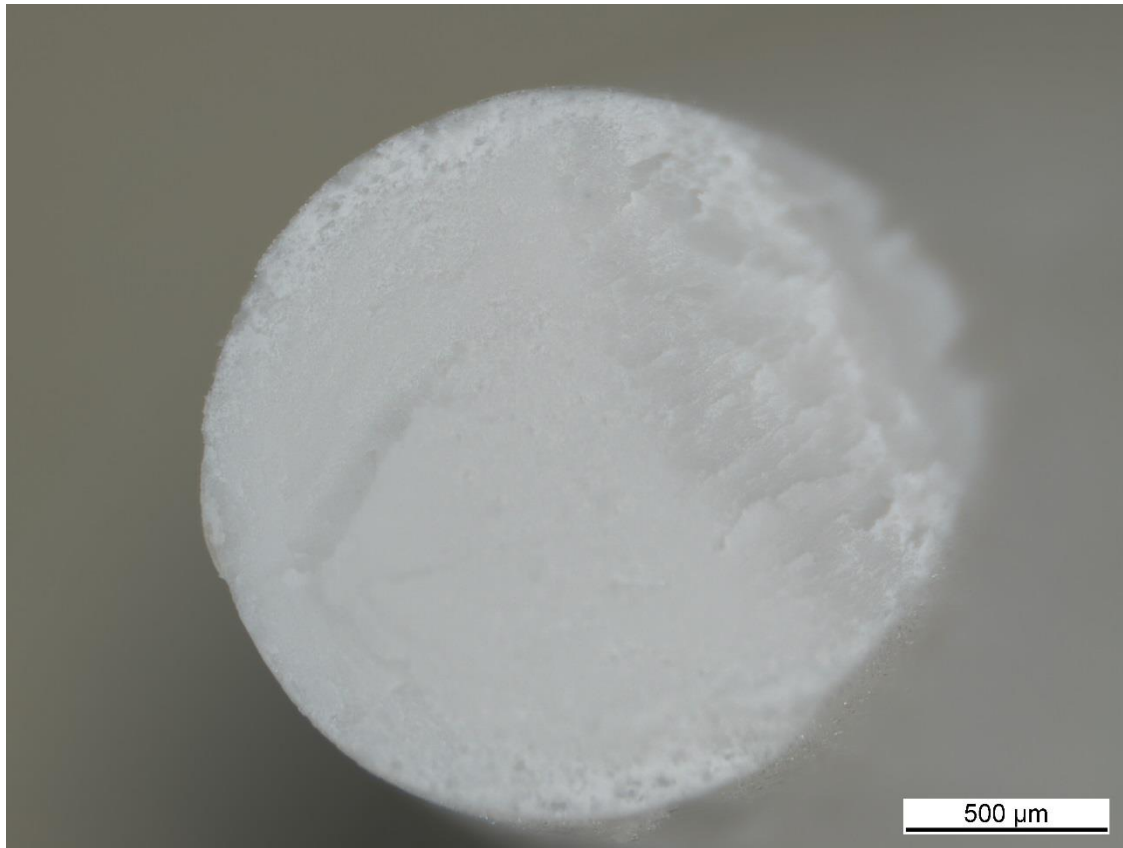


Figure S1: Image of a broken-off cross-section of the green filament.

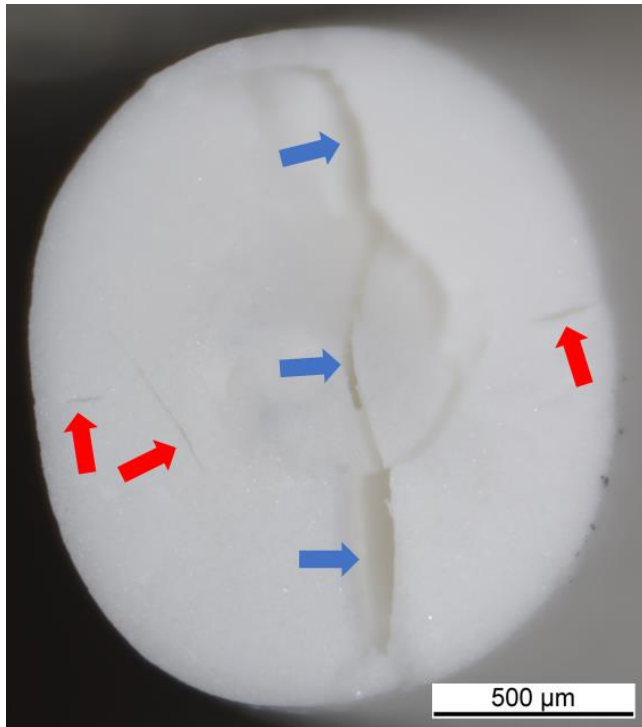


Figure S2: Image of the cross-section of a filament debound without a powder bed using the same thermal treatment as the other samples throughout this study. The blue arrows indicate a major crack through the whole diameter of the filament sample. The red arrows indicate minor cracks.

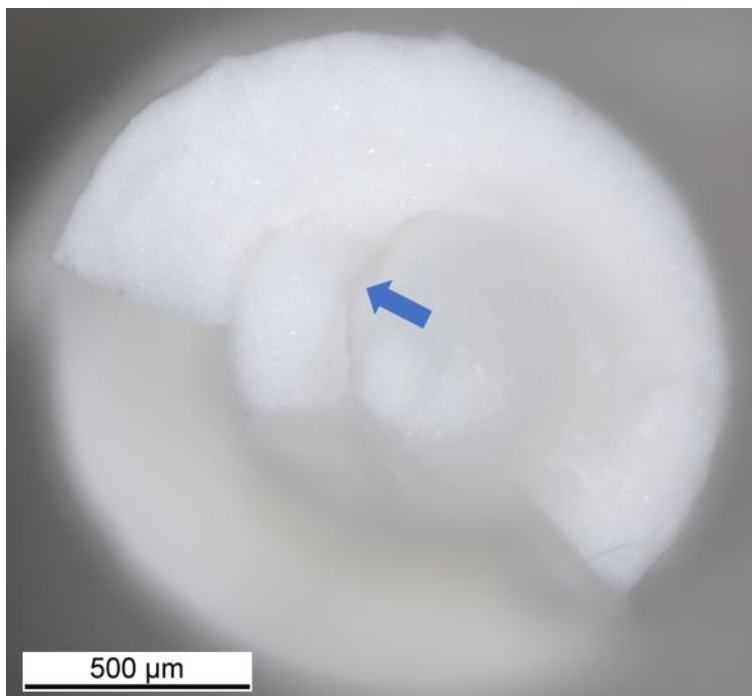


Figure S3: Image of the cross-section of a filament debound through the use of a powder bed while employing the same thermal treatment as with the other samples throughout this study. The blue arrow indicates a crack in the sample.